RSC Advances

PAPER

View Article Online
View Journal | View Issue

Cite this: *RSC Adv.*, 2025, **15**, 10754

Efficient photocatalytic degradation of methylene blue using 3D urchin-like TiO_2@rGO-hBN architecture†

Nguyen Thi Huyen,[ab] Tran Ai Suong Suong,[c] Cao Thi Thanh,[a] Nguyen Van Tu,[a] Pham Van Trinh,[a] Tran Van Tan,[d] Le Thi Quynh Xuan,[a] Bui Hung Thang,[a] Tran Van Hau,[a] Do Tuan,[a] Pham Duy Long,[a] Phan Ngoc Minh,[b] Hiroya Abe[e] and Nguyen Van Chuc *[ab]

3D urchin-like TiO_2@rGO-hBN architectures were produced by a hydrothermal method, followed by a cold plasma jet process. The morphology, crystal structure, composition and photocatalytic performance of the 3D urchin-like TiO_2@rGO-hBN architectures towards methylene blue (MB) were evaluated using SEM, Raman, XRD, EDS and UV-vis-NIR spectrophotometry. The obtained results indicated that under the same conditions, the MB degradation efficiencies were ~72%, ~81%, ~87%, and ~98% for 3D urchin-like TiO_2, 3D urchin-like TiO_2@rGO, 3D urchin-like TiO_2@hBN, and 3D urchin-like TiO_2@rGO-hBN, respectively, within 70 min under ultraviolet (UV) light irradiation with a wavelength of 365 nm. The significantly improved MB degradation efficiency was attributed to the effective separation of electron–hole pairs and the formation of ternary heterojunctions based on TiO_2, rGO and hBN. The results show the promising potential of 3D urchin-like TiO_2@rGO-hBN for applications in the photocatalytic degradation of organic pollutants.

Received 5th February 2025
Accepted 22nd March 2025

DOI: 10.1039/d5ra00845j

rsc.li/rsc-advances

1. Introduction

The escalating issue of water pollution, especially from industrial effluents, has drawn global attention due to its severe impact on ecosystems and public health. Among the various pollutants, synthetic dyes, such as methylene blue (MB), are particularly problematic because of their toxic, carcinogenic, and non-biodegradable nature.[1] These dyes are widely used in industries, such as textiles, plastics, and cosmetics, where they often end up in water bodies, causing significant environmental hazards.[1–3] As traditional water treatment methods are not fully effective in removing dyes, there is an urgent need for innovative solutions to tackle these pollutants in a sustainable and efficient manner.

Recent advancements in photocatalysis have opened new avenues for treating dye-contaminated wastewater by utilizing sunlight or artificial light to degrade harmful organic compounds.[4] Photocatalysis is classified into two types: homogeneous and heterogeneous.[5] In homogeneous photocatalysis, the catalyst and reactants are in the same phase, typically in a solution. In contrast, heterogeneous photocatalysis uses a solid catalyst in a different phase from the reactants, usually in a liquid or gas mixture.[6] This type offers the advantage of allowing the catalyst to be easily recovered and reused, making it more cost-effective and sustainable.[5] Titanium dioxide (TiO_2) is a widely used heterogeneous photocatalyst due to its non-toxic nature, abundance, strong oxidative capabilities, chemical stability, high redox potential, and low cost.[2,7–9] Its ability to generate reactive oxygen species (ROS) under ultraviolet (UV) irradiation makes it highly effective for degrading organic pollutants, including dyes.[10] Despite these advantages, TiO_2's practical application in environmental remediation is limited by its wide bandgap (3.2 eV), restricting its absorption to the UV region, which accounts for only a small fraction of the solar spectrum.[2,3,8] Additionally, rapid recombination of photogenerated electron–hole pairs reduces its overall efficiency.[11] As a result, there has been substantial interest in modifying TiO_2 or combining it with other materials to overcome these limitations and enhance its photocatalytic performance. TiO_2 has been combined with one or more materials to improve its photocatalytic ability.

With high surface area, suitable band gap, superior chemical and physical properties, high carrier mobility and a two-

[a]*Institute of Materials Science, Vietnam Academy of Science and Technology, 18 Hoang Quoc Viet, Cau Giay, Hanoi, Vietnam. E-mail: chucnv@ims.vast.vn*
[b]*Graduate University of Science and Technology, Vietnam Academy of Science and Technology, 18 Hoang Quoc Viet, Cau Giay, Hanoi, Vietnam*
[c]*VNU University of Engineering and Technology, 144 Xuan Thuy, Cau Giay, Hanoi, Vietnam*
[d]*Faculty of Physics, University of Science, Vietnam National University, 334 Nguyen Trai, Thanh Xuan, Hanoi, Vietnam*
[e]*Joining and Welding Research Institute, Osaka University, Osaka 5670047, Japan*

† Electronic supplementary information (ESI) available. See DOI: https://doi.org/10.1039/d5ra00845j

dimensional (2D) structure, materials like graphene, hexagonal boron nitride (hBN) and molybdenum disulfide (MoS_2) have received special attention from scientists in photocatalytic applications for environmental treatment.[3,12–15] When combined with TiO_2, 2D materials act as electron acceptors, helping to minimize the recombination of electron–hole pairs and supporting active sites for the reaction. R. Jain *et al.* found that TiO_2 nanoparticles supported on rGO sheets display enhanced photocatalytic features due to the rapid molecular diffusion of water and MB molecules within the mesoporous structure of crystalline/amorphous heterojunctions in the TiO_2/Ex-rGO composite.[3] Compared to bare TiO_2, TiO_2/Ex-rGO composite has a photodegradation rate for MB that is 2.38 times higher.[3] L. Chen *et al.* showed that, compared with bare TiO_2, the MoS_2/TiO_2 nanocomposite fabricated by the hydrothermal method increased MB photocatalytic degradation by 3.8 times.[13] D. Liu *et al.* reported that the porous BN/TiO_2 composite nanosheet exhibits enhanced photocatalytic degradation of rhodamine B (RhB) compared to pure TiO_2 due to the large number of highly chemically active Ti–O–B chemical bonds formed between B and TiO_2 in the composite. The Ti–O–B bonds in the nanocomposites facilitate electron transfer from TiO_2 to hBN, leading to a narrower bandgap of h-BN/TiO_2.[14] Recently, V. Yadav *et al.* showed that the insertion of GO into hBN nanosheets enhances the photocatalytic degradation of methyl orange (MO) compared to bare hBN or GO due to the formation of a potential barrier at the GO-hBN interface and the reduced band gap of the GO-hBN nanocomposite. These factors help enhance two-photon absorption, separate charge carriers and reduce electron–hole recombination.[16] S. Al-Kandari *et al.* synthesized a BNrGO-TiO_2 nanocomposite by the hydrothermal method and used it as a high-performance photocatalyst in the photodegradation of phenol.[4] Therefore, the combination of TiO_2 with the rGO-hBN composite can be considered as one of the photocatalyst starting materials for the degradation of organic pollutants. However, most of the synthesized samples are in powder form, which limits the ability to recover the product after photocatalytic degradation.

Motivated by the above analysis, this study aims to develop a novel 3D urchin-like TiO_2@rGO-hBN composite architecture on silicon substrates with enhanced photocatalytic properties and good recoverability for the degradation of MB. The unique 3D structure is expected to increase the active surface area for photocatalysis, while the integration of rGO and hBN will improve charge transfer and reduce the recombination of photogenerated electron–hole pairs. This combination seeks to address the challenges faced by conventional TiO_2-based photocatalysts and achieve efficient degradation of organic pollutants under UV light irradiation.

2. Materials and methods

2.1. Materials

Titanium tetrachloride ($TiCl_4$, 99%), hydrochloric acid (HCl, 37%), methylene blue (MB, 99%), isopropyl alcohol (IPA, >99%), benzoquinone (BQ, 99%) and ethylenediaminetetraacetic acid disodium (EDTA, 99%) were purchased from Macklin Co. Ltd (China). Graphene oxide (GO) with sizes of several micrometers (Fig. S1†) and boron nitride (BN) sheets with sizes of several tens of nanometers (Fig. S2†) were fabricated by the Hummers' method[17] and ball milling method,[18] respectively.

2.2. Fabrication of 3D urchin-like TiO_2, TiO_2@rGO and TiO_2@rGO-hBN architectures

3D urchin-like TiO_2 architectures were synthesized on silicon substrates *via* a hydrothermal process. Firstly, 8 mL of 37% HCl was mixed with 4 mL of deionized water, followed by the addition of 0.3 mL titanium tetrachloride ($TiCl_4$, 99%) under continuous stirring for 20 min at a temperature of 7–10 °C using an ice bath. Next, the resulting solution was transferred to a 50 mL stainless steel autoclave, with the silicon substrates (measuring 0.5 cm × 0.5 cm) placed horizontally at the bottom of the autoclave. The autoclave was then heated to 160 °C and maintained for 6 h, before being allowed to cool naturally to room temperature. After that, the obtained samples were collected, washed with deionized water, dried at 50 °C for 60 min, and calcined at 400 °C for 1 h in air to obtain 3D urchin-like TiO_2 samples. For the preparation of 3D urchin-like TiO_2@rGO architectures, 10 μL of GO solution (0.25 mg mL^{-1}), prepared by the Hummers' method, was dropped onto the surface of the TiO_2 at room temperature, followed by cold plasma jet treatment for 3 min in Ar gas with a flow rate of 0.5 L min^{-1}. The detailed information about the configuration of the cold plasma jet was presented by Xuan *et al.* (2022).[19] The as-prepared samples were dried naturally for 24 h and annealed at 200 °C in air atmosphere. For the preparation of 3D urchin-like TiO_2@rGO-hBN architectures, the fabrication steps were performed similarly to those of the 3D urchin-like TiO_2@rGO architectures, with 10 μL of GO solution replaced by 10 μL of GO/hBN mixture solution with a volume ratio of 1 : 2.

2.3. Photocatalytic activity measurement

The absorption and photocatalytic activity of 3D urchin-like TiO_2, TiO_2@rGO and TiO_2@rGO-hBN architectures on silicon substrates were evaluated by measuring the degradation rate of MB solution under ultraviolet (UV) light irradiation with a wavelength of 365 nm. The obtained photocatalyst substrates were immersed in 20 mL of MB solution (10^{-5} M) for 1 h in the dark to reach the absorption/desorption equilibrium. The samples were then irradiated at fixed time intervals, and a volume of 3 mL of the reaction solution was withdrawn for each measurement of MB degradation.

2.4. Apparatus

The morphological features, presence of elements and structures of 3D urchin-like TiO_2, TiO_2@rGO and TiO_2@rGO-hBN architectures were characterized using scanning electron microscopy (FESEM, Hitachi S-4800, Japan), energy dispersive X-ray spectroscopy (EDS) attached to SEM (JSM-IT800, JOEL, Japan), Raman microscopy and X-ray diffraction (XRD D8 Advance, Bruker, Germany). The absorption and photocatalytic activities of the samples were measured at room temperature using a UV-vis spectrophotometer (UV-2450, Shimadzu, Japan).

3. Results and discussions

Fig. 1a shows the SEM image of 3D urchin-like TiO_2 synthesized after hydrothermal process. Fig. 1b and c show the SEM images of TiO_2@rGO and TiO_2@rGO-hBN nanocomposites synthesized after cold plasma treatment process, respectively. The SEM image of the TiO_2 sample (Fig. 1a) showed a 3D urchin shape with an average diameter of about 10 μm to 12 μm. The mechanism for the formation of the 3D urchin-like TiO_2 structure may follow a process of nucleation, dissolution, recrystallization and self-assembly, as presented in previous reports.[20,21] In the initial stage, amorphous or rutile TiO_2 nuclei were formed, which then coalesced into crinkly spherical units. As the reaction time increased, these TiO_2 spherical units dissolved and recrystallized to form TiO_2 nanoneedles on the surface of the microspheres. Subsequently, the TiO_2 nanoneedles began to directly self-assemble to form 3D urchin-like TiO_2 structures. In the case of TiO_2@rGO (Fig. 1b), the rGO sheets were homogeneously dispersed between the TiO_2 nanoneedles. It could be clearly seen that the restacking phenomenon of the rGO sheets was less pronounced. The rGO sheets appeared as thin ribbons that interconnected the TiO_2 nanoneedles, forming a composite material of rGO-wrapped 3D urchin-like TiO_2. In the case of TiO_2@rGO-hBN (Fig. 1c), the hBN nanosheets were also uniformly dispersed within the rGO matrix and coated onto the surface of TiO_2 after the cold plasma jet process. To further confirm the successful decoration of the rGO-hBN nanocomposite on TiO_2, Raman spectra of the hBN, GO, TiO_2, TiO_2@rGO and TiO_2@rGO-hBN samples were measured.

Fig. 1d shows the Raman spectra of hBN, GO, TiO_2, TiO_2@rGO and TiO_2@rGO-hBN. For hBN nanosheets, a band at ~1368 cm^{-1} was assigned to the in-plane vibration of the nitrogen and boron atoms (E_{2g}).[22] For GO nanosheets, two bands at ~1348 cm^{-1} and ~1600 cm^{-1} were assigned to the disorder band (D) and the graphite band (G).[17] For 3D urchin-like TiO_2, two characteristic peaks were observed at ~443 cm^{-1} and ~608 cm^{-1}, corresponding to the E_g and A_{1g} active modes of the rutile phase.[23,24] The Raman spectrum of the 3D urchin-like TiO_2@rGO nanocomposite showed the characteristic peaks of the TiO_2 rutile phase (at ~443 cm^{-1} and ~608 cm^{-1}) and graphene (at ~1348 cm^{-1} and ~1600 cm^{-1}). The defect levels of graphene could be estimated *via* the intensity ratio between the D and G bands (I_D/I_G).[25,26] Compared to pure GO, the I_D/I_G ratio of TiO_2@rGO increased from 0.95 to 1.32, demonstrating that GO had been reduced to rGO during the jet plasma process.[27] For the 3D urchin-like TiO_2@rGO-hBN, it could be clearly seen that all the characteristic Raman peaks of the TiO_2 rutile phase (at ~443 cm^{-1} and ~608 cm^{-1}) and graphene (at ~1348 cm^{-1} and ~1600 cm^{-1}) were observed. The

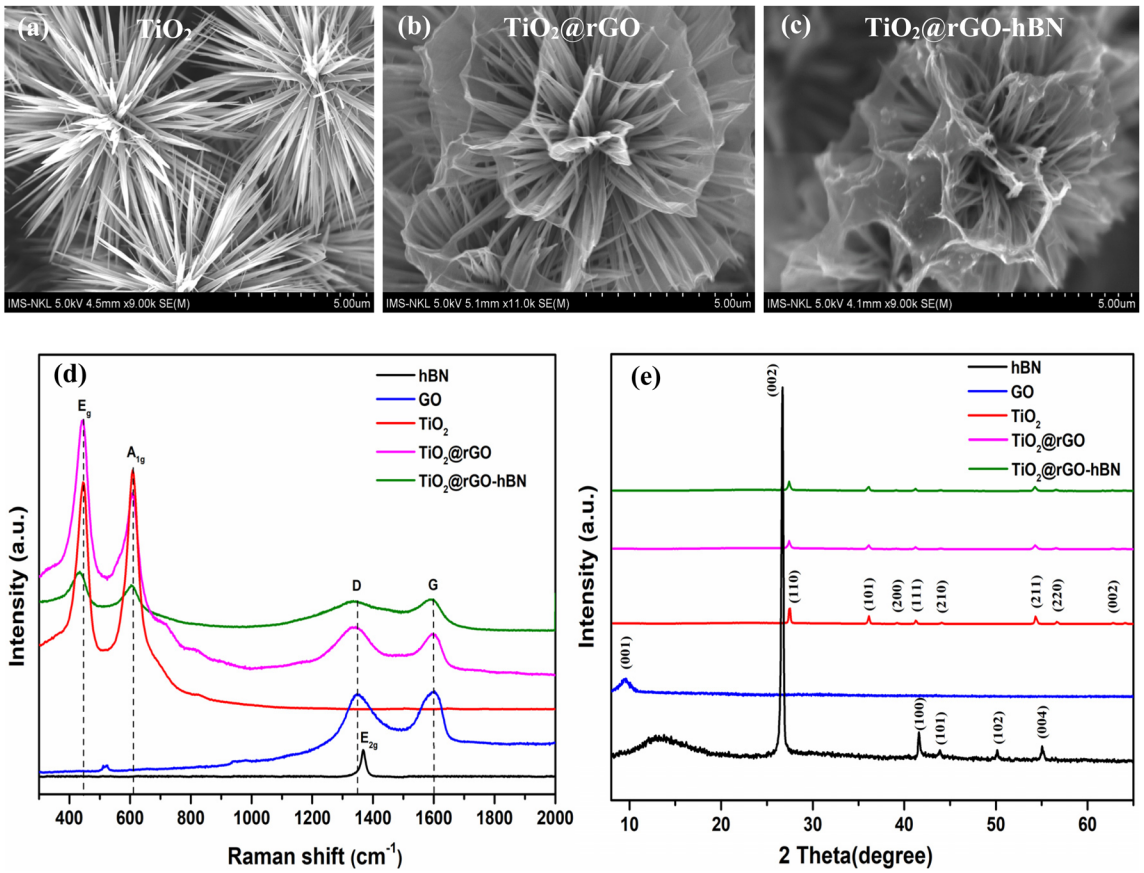

Fig. 1 SEM images of (a) TiO_2, (b) TiO_2@rGO and (c) TiO_2@rGO-hBN. Raman spectra (d) and XRD pattern (e) of hBN, GO, TiO_2, TiO_2@rGO and TiO_2@rGO-hBN.

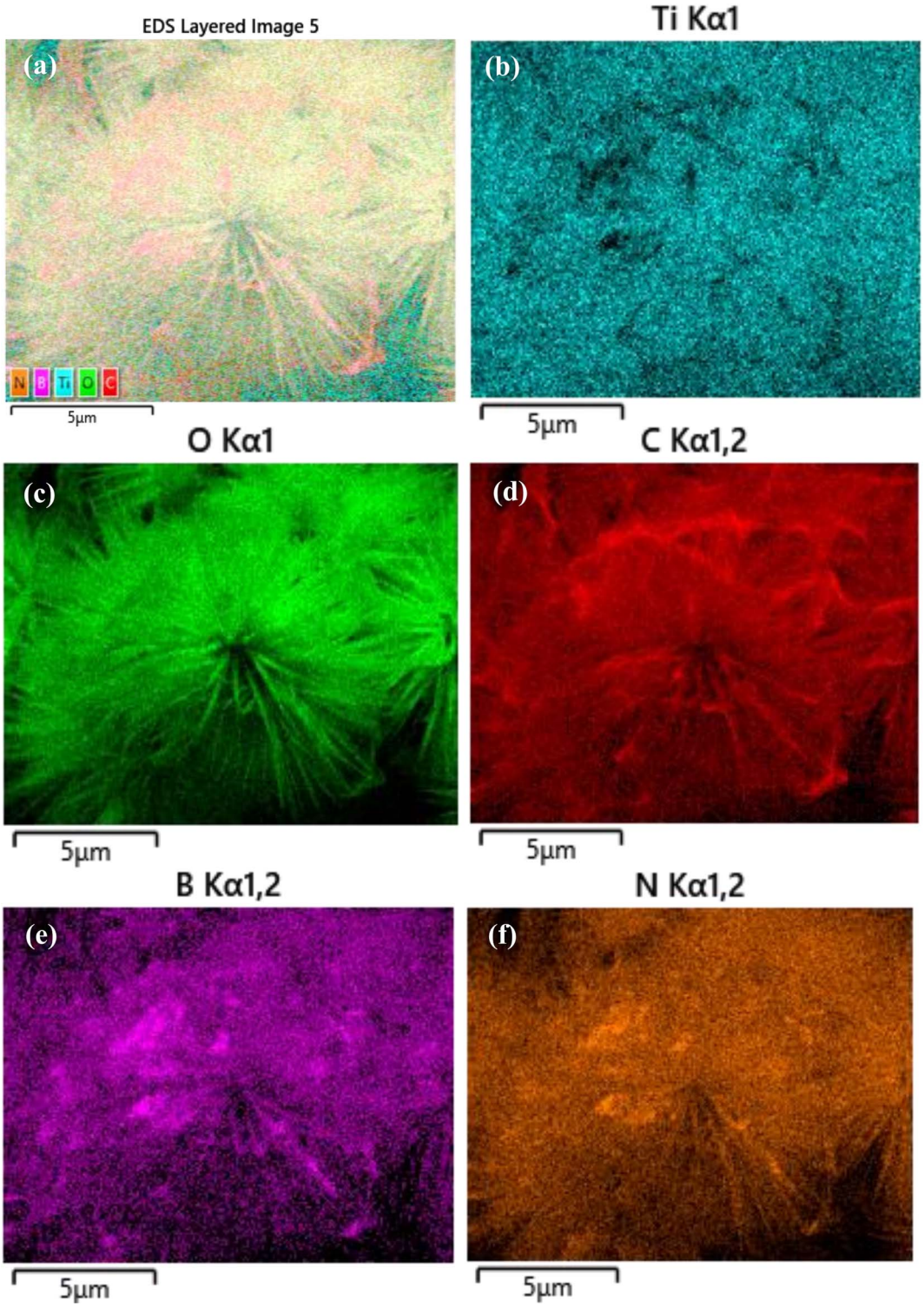

Fig. 2 (a) SEM mapping image and elemental mapping images of (b) Ti, (c) O, (d) C, (e) B and (f) N elements of TiO_2@rGO-hBN.

characteristic peak of hBN at ~1368 cm^{-1} was not distinctly discernible in TiO_2@rGO-hBN, possibly due to its blending with the D band of rGO.

The XRD patterns were obtained to determine the crystal structure and phase of the samples. As shown in Fig. 1e, for hBN, diffraction peaks were observed at 2θ angles of 26.6°, 41.6°, 44.0°, 50.1° and 55.1°, corresponding to the (002), (100), (101), (102) and (004) crystal planes of hBN (JCPDS 01-073-2095).[28] GO nanosheets showed a characteristic diffraction peak at $2\theta = 10.6°$, corresponding to the (001) plane.[29] For 3D urchin-

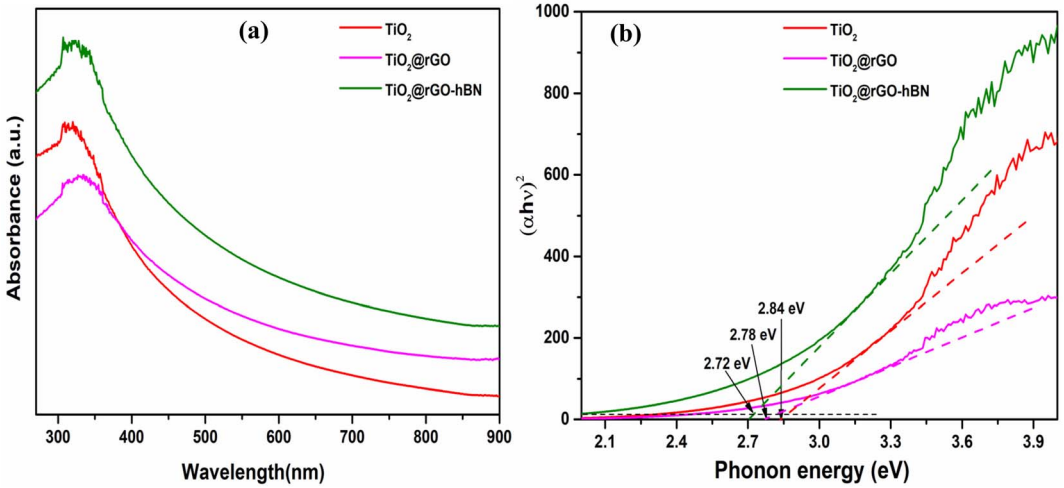

Fig. 3 (a) UV-vis absorption spectra and (b) optical band gap of TiO_2, TiO_2@rGO and TiO_2@rGO-hBN.

like TiO_2, the diffraction peaks at 2θ values of 27.4°, 36.1°, 39.2°, 41.3°, 44.1°, 54.4°, 56.7° and 62.8° were indexed to the (110), (101), (200), (111), (210), (211), (220), and (002) planes of rutile TiO_2 crystal (JCPDS No. 01-087-0710).[30] For the 3D urchin-like TiO_2@rGO and TiO_2@rGO-hBN nanocomposites, all the characteristic diffraction peaks of rutile TiO_2 were clearly observed.

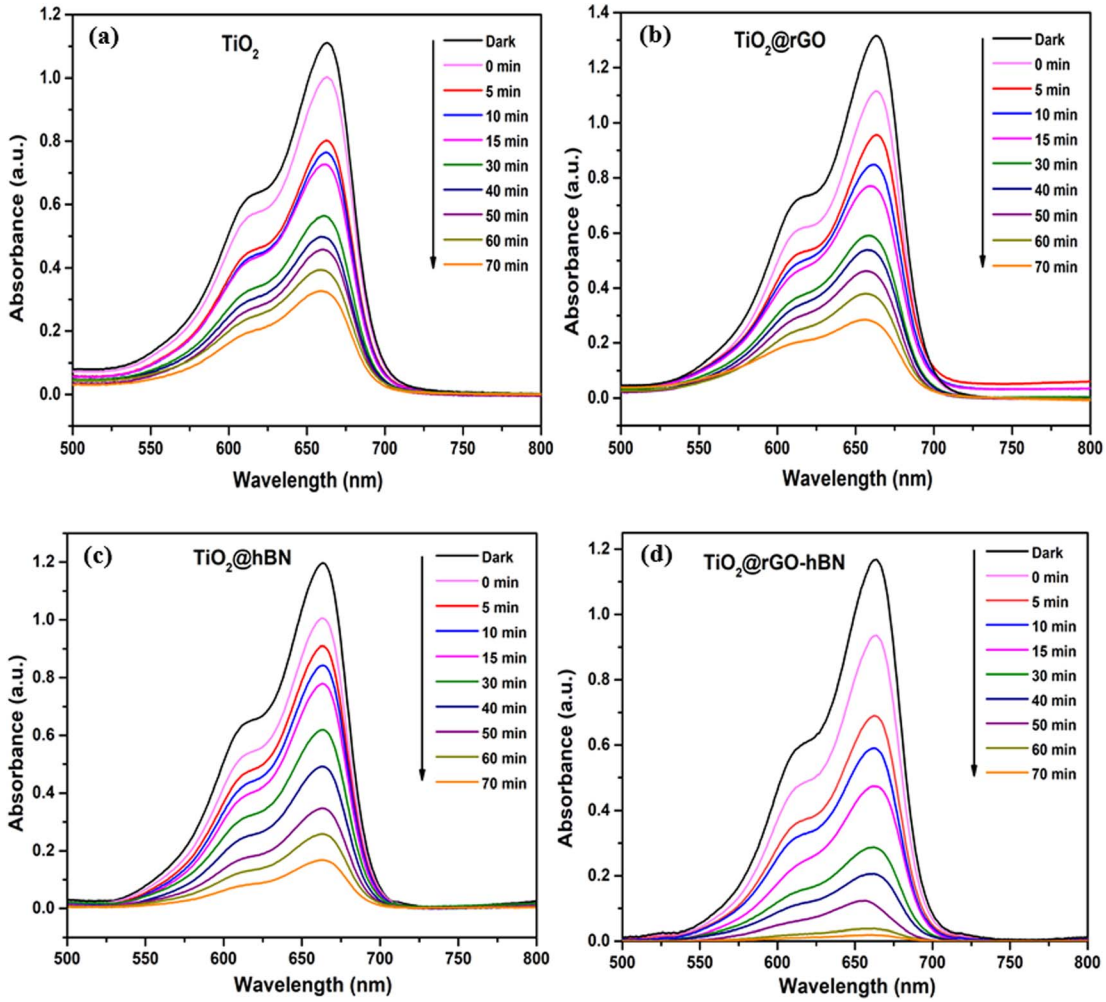

Fig. 4 Photodegradation absorption spectra of MB solution in (a) TiO_2, (b) TiO_2@rGO, (c) TiO_2@hBN and (d) TiO_2@rGO-hBN.

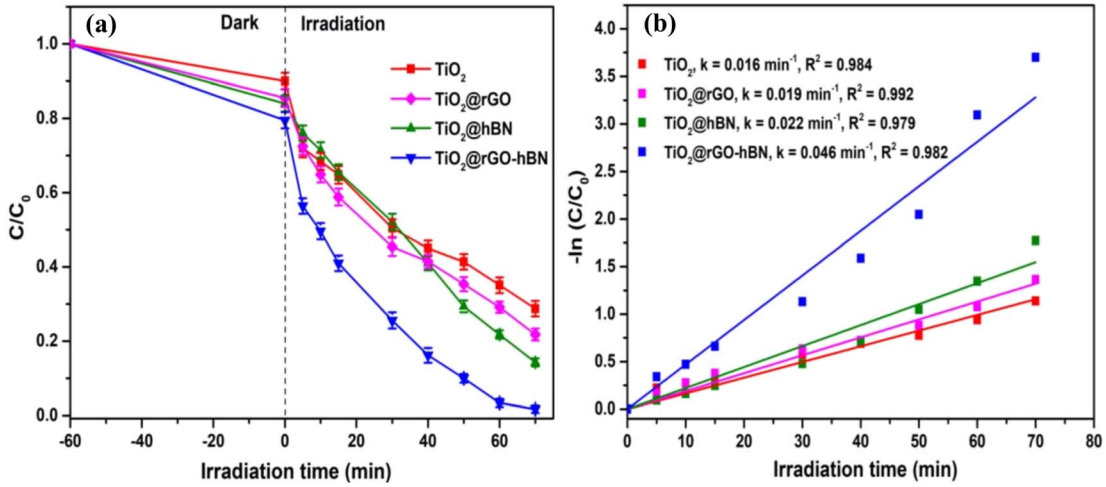

Fig. 5 Comparison of (a) photocatalytic activity and (b) apparent rate constants (k) of TiO_2, TiO_2@rGO, TiO_2@hBN and TiO_2@rGO-hBN towards photocatalytic degradation of MB solution under UV light irradiation.

Meanwhile, the characteristic diffraction peaks of rGO and hBN were not observed due to the high density, large size and crystallinity of the 3D urchin-like TiO_2. The architectural shape of the 3D urchin-like TiO_2@rGO-hBN and the uniform distribution of the elements Ti, O, C, B and N were confirmed by SEM and EDS mapping. The SEM-EDS mapping of 3D urchin-like TiO_2@rGO-hBN showed the elements distribution of Ti, O, C, B, and N, corresponding to the sky blue, green, red, purple, and orange colors, as shown in Fig. 2.

Fig. 3a shows the UV-visible absorption spectra of TiO_2, TiO_2@rGO and TiO_2@rGO-hBN samples recorded in the range of 280 nm to 900 nm. Compared to pure TiO_2 and TiO_2@rGO, the visible light absorption of TiO_2@rGO-hBN nanocomposites was increased. The increased visible light absorption of the TiO_2@rGO-hBN nanocomposites could improve the generation of more electron–hole pairs, contributing to the enhancement of photocatalytic activities. The optical band gaps of bare TiO_2, TiO_2@rGO and TiO_2@rGO-hBN composites were estimated to be about 2.84, 2.78 and 2.72 eV, respectively, from a plot of $(\alpha h\nu)^2$ *vs.* phonon energy (eV), as shown in Fig. 3b. The reduced band gap energy and improved light absorption in the visible light region were beneficial for the generation of photoexcited charge carriers, thus improving efficient photocatalytic reactions under visible light irradiation.

The photocatalytic degradation of MB over TiO_2, TiO_2@rGO, TiO_2@hBN and TiO_2@rGO-hBN samples under UV light irradiation (365 nm) was evaluated by measuring the UV-vis absorption spectrum at different UV irradiation times. As shown in Fig. 4, two characteristic absorption peaks of MB for four samples were observed at about 663 nm and 613 nm, and these peaks were related to the monomer and dimer of MB, respectively. The longer the UV irradiation time, the lower the UV-vis signal intensity of the MB dye. The decrease in absorption intensity indicated the degradation of MB. Since the intensity of the MB absorption spectrum peak was proportional to MB concentration,[31–33] the relative change in MB concentration (C/C_0) due to photocatalytic degradation could be monitored over time by measuring the main peak intensity at 663 nm

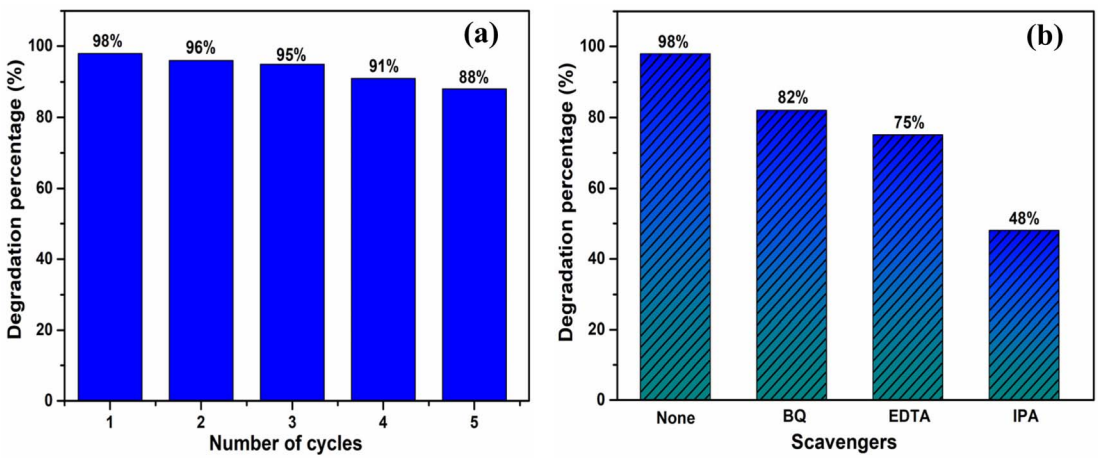

Fig. 6 (a) Recycling performance and (b) trapping experiment for photocatalytic degradation of MB solution over TiO_2@rGO-hBN under UV light irradiation.

Table 1 Comparison of photocatalytic degradation of MB under UV irradiation sources[a]

Catalyst	Irradiation source	Evaluation method	Time (min)	Degradation efficiency (%)	Degradation rate (min^{-1})	Ref.
AuNPs-TiO_2 NTs	UV (254 nm, 15 W)	Raman	80	100	5.1×10^{-2}	36
TiO_2/BNNS NRs	UV (254 nm, 66 W)	Raman	50	100	8.5×10^{-2}	18
F–TiO_2	UV (>400 nm, 400 W)	PL	240	91.0	—	37
TiO_2 particles	UV (254 nm, 360 W)	UV-vis	40	54.69	2.3×10^{-2}	38
F-BN/TiO_2	UV (420 nm)	UV-vis	120	90.5	—	39
ZnO–TiO_2/rGO	UV	UV-vis	63.5	99.4	7.07×10^{-2}	40
NiCd TiO_2	UV (254 nm, 15 W)	UV-vis	100	86.0	—	41
hBN/TiO_2 powder	UV (365 nm)	UV-vis	50	92.0	4.98×10^{-2}	42
rGO-TiO_2/SA/PAM	Mercury lamp (200 W)	UV-vis	100	97.14	3.628×10^{-2}	43
ZT-rGO	UV (365 nm)	UV-vis	30	98.5	1.49×10^{-1}	44
TiO_2/Ex-rGO	UV lamp (750 W)	UV-vis	160	92.1	6.455×10^{-2}	3
TiO_2 film	UV (254 nm)	UV-vis	480	97.0	7.8×10^{-3}	45
NiO/TiO_2	UV (365 nm)	UV-vis	60	25.3	4.93×10^{-3}	46
BNMT-BNNS/TiO_2	UV (<400 nm)	UV-vis	115	99.62	—	47
TiO_2@rGO-hBN	UV (365 nm)	UV-vis	70	~98	4.6×10^{-2}	This work

[a] AuNPs, gold nanoparticles; NiCd, nickel cadmium; F-BN, fluorinated hexagonal boron nitride; PL, photoluminescence; SA, sodium alginate; PAM, polyacrylamide; ZT: ZnO–TiO_2; Ex-rGO, exfoliated rGO; BNMT, boron nitride micron square tubes; BNNS, boron nitride nanosheets.

after TiO_2, TiO_2@rG, TiO_2@hBN and TiO_2@rGO-hBN samples were immersed in the MB solution. Fig. 5a shows that TiO_2@rGO-hBN exhibited a photocatalytic degradation efficiency of about ~98%, which was higher than that of TiO_2@hBN (~87%), TiO_2@rGO (~81%) and TiO_2 (~72%). The degradation rate constants (k) of MB were calculated from the pseudo-first-order reaction using the graph of $-\ln(C/C_0)$ *vs.* irradiation time. As shown in Fig. 5b, the rate constants for TiO_2, TiO_2@rGO, TiO_2@hBN and TiO_2@rGO-hBN were estimated to be 0.016 min^{-1}, 0.019 min^{-1}, 0.022 min^{-1}, and 0.046 min^{-1} for MB dye. The degradation efficiency of TiO_2@rGO-hBN under UV lamp irradiation was also carefully evaluated over five cycles, as

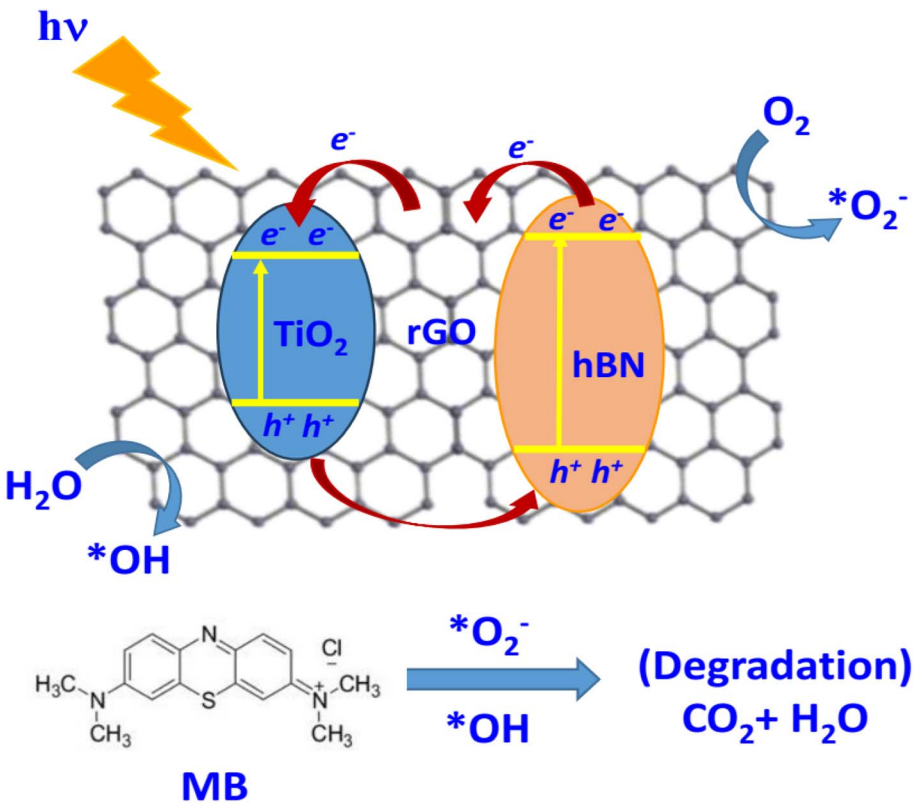

Fig. 7 Degradation mechanism of TiO_2@rGO-hBN towards MB.

shown in Fig. 6a. The degradation percentages of TiO_2@rGO-hBN for MB molecules after the 1st, 2nd, 3rd, 4th and 5th cycles were estimated to be ~98%, ~96%, ~95%, ~91% and ~88%, respectively. Additionally, the recoverability of TiO_2@rGO-hBN after photocatalytic degradation was close to 100%. These results demonstrated the high recycling performance of the TiO_2@rGO-hBN material. Compared with previously reported materials for the photocatalytic degradation of MB under UV irradiation sources, as shown in Table 1, the 3D urchin-like TiO_2@rGO-hBN architectures demonstrated promising potential for applications in the photocatalytic degradation of organic pollutants.

The significant improvement in the photocatalytic performance of TiO_2@rGO-hBN for MB molecules could be explained by the existence of a heterogeneous structure and the large surface area of the rGO-hBN nanocomposite on the surface of TiO_2. The large surface area and numerous interfaces of TiO_2@rGO-hBN were beneficial for the adhesion of MB molecules, enhancing the photocatalytic performance. To identify the radical scavengers, three different capturing agents, including isopropyl alcohol (IPA),[1] ethylenediaminetetraacetic acid disodium (EDTA),[1] and benzoquinone (BQ),[34] were introduced into the reaction mixture. IPA, EDTA, and BQ were used to trap hydroxyl radicals (*OH), holes (h^+), and superoxide radicals ($*O_2^-$), respectively. As shown in Fig. 6b, in the presence of BQ, EDTA, and IPA, the degradation of MB under UV light irradiation decreased from 98% to 82%, 75%, and 48%, respectively. These results suggested that *OH radicals played an important role in the decomposition of MB, while h^+ and $*O_2^-$ played a relatively minor role in MB photodecomposition.

The photocatalytic mechanism of TiO_2@rGO-hBN for MB degradation is shown in Fig. 7. Under ultraviolet light irradiation, excited electrons (e^-) from the surface of hBN were rapidly transferred from the valence band (VB) of hBN to the conduction band (CB), generating electron–hole (e^-–h^+) pairs. The photogenerated e^- in the CB of hBN could move from hBN to rGO, and then these e^- would continue to move to the CB of TiO_2. The rGO nanosheets acted as "transport bridges" between the photocatalysts and improved the ability to effectively separate photogenerated e^-–h^+ pairs due to their superior conductivity.[12,35] Meanwhile, the large surface area of hBN was also beneficial for dye attachment.[16] As a result, the electrons and holes reacted with dissolved oxygen (O_2) and water (H_2O) molecules to generate superoxide anions ($*O_2^-$) and hydroxyl radicals (*OH). The h^+, $*O_2^-$ and *OH activated radicals degraded the MB molecules adsorbed on the surface of the photocatalyst into CO_2 and H_2O under UV light irradiation.

4. Conclusions

In this work, 3D urchin-like TiO_2@rGO-hBN architectures on silicon substrates were fabricated by a hydrothermal method, followed by the deposition of rGO-hBN nanocomposites onto the surface of 3D urchin-like TiO_2 using a cold plasma jet process. The 3D urchin-like TiO_2@rGO-hBN architectures were used as candidates for photocatalytic degradation of MB. The obtained results indicated that the MB degradation efficiency was about 98% within 70 min under UV light irradiation (365 nm). The significantly improved MB degradation efficiency was attributed to the effective separation of electron–hole pairs and the formation of ternary heterojunctions based on TiO_2, rGO and hBN.

Data availability

The datasets used and/or analyzed during the current study are available from the corresponding author upon reasonable request. In addition, all the data generated or analyzed during this study are included in this article.

Author contributions

Nguyen Thi Huyen: conceptualization, methodology, investigation, formal analysis. Tran Ai Suong Suong: conceptualization, methodology, investigation. Cao Thi Thanh: formal analysis, investigation. Nguyen Van Tu: formal analysis, investigation. Pham Van Trinh: formal analysis, investigation. Tran Van Tan: formal analysis, investigation. Le Thi Quynh Xuan: formal analysis, investigation. Bui Hung Thang: formal analysis, investigation. Tran Van Hau: formal analysis, investigation. Do Tuan: formal analysis, investigation. Pham Duy Long: investigation. Phan Ngoc Minh: supervision, investigation. Hiroya Abe: supervision, investigation. Nguyen Van Chuc: supervision, conceptualization, methodology, formal analysis, project administration, writing – original draft preparation, validation, writing – reviewing and editing. All authors discussed and approved the manuscript.

Conflicts of interest

There are no conflicts to declare.

Acknowledgements

This work was financially supported by the Vietnam Academy of Science and Technology (VAST) under Project NCXS02.03/24-25.

References

1 R. Nilmadhab, T. Nivedya, P. Priyankar and C. Rinku, *RSC Adv.*, 2025, **15**, 3008–3025.
2 M. Kocijan, L. Curkovíc, D. Ljubas, K. Mužina, I. Bǎcíc, T. Radoševíc, M. Podlogar, I. Bdikin, G. O. Irurueta, M. J. Hortigüela and G. Gonçalves, *Appl. Sci.*, 2021, **11**, 3966.
3 R. Jain, M. Upadhyaya, A. Singh and R. P. Jaiswal, *J. Environ. Chem. Eng.*, 2024, **12**, 113881.
4 S. Al-Kandari, A. M. Abdullah, H. Al-Kandari, G. K. Nasrallah, M. A. Sharaf, D. S. Al-Marzouq, A. M. Mohamed, N. Younes, N. Kafour and T. Al-Tahtamouni, *Environ. Sci. Pollut. Res.*, 2021, **28**, 62771–62781.
5 S. Khan, T. Noor, N. Iqbal and L. Yaqoob, *ACS Omega*, 2024, **9**, 21751–21767.
6 N. Akechatree, R. Rajendran, T. Rojviroon, P. Arumugam, V. Vasudevan, S. Sirivithayapakorn, A. Dhayalan,

P. Wongpipun, N. Phetyim and O. Rojviroon, *Mater. Res. Bull.*, 2025, **181**, 113119.
7 G. Ali, I. Ali, M. A. Marwat, J. Khan, M. A. Basit and T. J. Park, *Chem. Phys. Lett.*, 2024, **848**, 141372.
8 H. Atout, M. G. Álvarez, D. Chebli, A. Bouguettoucha, D. Tichit, J. Llorca and F. Medina, *Mater. Res. Bull.*, 2017, **95**, 578–587.
9 L. Jiang, W. Wei, S. Liu, S. A. Haruna, M. Zareef, W. Ahmad, Md. M. Hassan, H. Li and Q. Chen, *J. Food Meas. Charact.*, 2022, **16**, 2890–2898.
10 H. Y. Ma, L. Zhao, L. H. Guo, H. Zhang, F. J. Chen and W. C. Yu, *J. Hazard. Mater.*, 2019, **369**, 719–726.
11 T. Gupta, Samriti, J. Cho and J. Prakash, *Mater. Today Chem.*, 2021, **20**, 100428.
12 Y. Ren, Y. Dong, Y. Feng and J. Xu, *Catalysts*, 2018, **8**, 590.
13 L. Chen, S. F. Ou, T. B. Nguyen, Y. Chuang, C. W. Chen and C. D. Dong, *J. Taiwan Inst. Chem. Eng.*, 2025, **166**, 105436.
14 D. Liu, M. Zhang, W. Xie, L. Sun, Y. Chen and W. Lei, *Appl. Catal., B*, 2017, **207**, 72–78.
15 W. Zhang, Y. Xu and X. Zou, *Food Chem.*, 2018, **261**, 1–7.
16 V. Yadav, M. K. Kumawat, S. Tiwari, A. K. Singh and T. Mohanty, *FlatChem*, 2024, **45**, 100659.
17 C. T. Thanh, N. H. Binh, P. N. D. Duoc, V. T. Thu, P. V. Trinh, N. N. Anh, N. V. Tu, N. V. Tuyen, N. V. Quynh, V. C. Tu, B. T. P. Thao, P. D. Thang, H. Abe and N. V. Chuc, *Bull. Environ. Contam. Toxicol.*, 2021, **106**, 1017–1023.
18 N. T. Huyen, N. V. Tu, T. V. Hau, P. V. Trinh, C. T. Thanh, N. T. Loan, T. V. Tan, N. V. Tuyen, V. D. Chinh, V. X. Hoa, C. T. Anh and N. V. Chuc, *Mater. Lett.*, 2023, **340**, 134213.
19 L. T. Q. Xuan, L. N. Nguyen and N. T. Dao, *Nanotechnology*, 2022, **33**, 105603.
20 L. Xiang, X. Zhao, J. Yin and B. Fan, *J. Mater. Sci.*, 2012, **47**, 1436–1445.
21 C. Shi, M. Eqi, J. Shi, Z. Huang and H. Qi, *J. Colloid Interface Sci.*, 2023, **650**, 1736–1748.
22 B. Yu, J. Fan, J. He, Y. Liu, R. Wang, K. Qi, P. Han and Z. Luo, *J. Alloys Compd.*, 2023, **930**, 167303.
23 D. Nunes, A. Pimentel, L. Santos, P. Barquinha, E. Fortunato and R. Martins, *Catalysts*, 2017, **7**, 60.
24 E. Perevedentseva, Y. C. Lin, A. Karmenyan, K. T. Wu, A. Lugovtsov, E. Shirshin, A. Priezzhev and C. L. Cheng, *Materials*, 2021, **14**, 5920.
25 P. N. D. Duoc, N. H. Binh, T. V. Hau, C. T. Thanh, P. V. Trinh, N. V. Tuyen, N. V. Quynh, N. V. Tu, V. D. Chinh, V. T. Thu, P. D. Thang, P. N. Minh and N. V. Chuc, *J. Hazard. Mater.*, 2020, **400**, 123185.
26 C. T. Thanh, N. T. Huyen, P. V. Trinh, N. V. Tu, V. T. Thu, V. C. Tu, D. N. Nhiem, P. T. Binh, N. N. Anh, V. X. Hoa, P. N. Minh, H. Abe and N. V. Chuc, *Diamond Relat. Mater.*, 2025, **152**, 111889.
27 N. T. Huyen, L. T. Q. Ngan, L. T. Q. Xuan, T. A. S. Suong, C. T. Thanh, N. V. Tu, P. T. Binh, T. V. Tan, N. V. Tuyen, D. T. Cao, P. V. Hai, V. X. Hoa and N. V. Chuc, *Opt. Mater.*, 2025, **162**, 116935.
28 N. K. Mahto, K. Shafali, R. Tyagi, O. P. Sharma, O. P. Khatri and S. K. Sinha, *Wear*, 2023, **530–531**, 205065.
29 F. Zhu, X. She, Z. Zhang, X. Yu, H. Huang, J. Ji, L. Li and S. Li, *J. Phys. Chem. Solids*, 2024, **195**, 112269.
30 S. Wannapop and A. Somdee, *Ceram. Int.*, 2020, **46**, 25758–25765.
31 S. Y. Lee, H. T. Do and J. H. Kim, *Appl. Surf. Sci.*, 2022, **573**, 151383.
32 S. A. Haladu, K. A. Elsayed, A. A. Manda, U. I. Gaya, M. A. Almessiere and M. A. Hafez, *Opt. Laser Technol.*, 2025, **180**, 111498.
33 N. T. K. Ngan, F. Grasset, S. Ishii, H. Fudouzi and T. Uchikoshi, *Mater. Adv.*, 2024, **5**, 8615–8628.
34 Z. Zhu, J. Ye, X. Tang, Z. Chen, J. Yang, P. Huo, Y. H. Ng and J. Crittenden, *Environ. Sci. Technol.*, 2023, **57**, 16131–16140.
35 Z. Zhu, Q. Han, D. Yu, J. Sun and B. Liu, *Mater. Lett.*, 2017, **209**, 379–383.
36 R. Li, A. Zhou, Q. Lu, C. Yang and J. Zhang, *Colloids Surf., A*, 2013, **436**, 270–278.
37 W. Yu, X. Liu, L. Pan, J. Li, J. Liu, J. Zhang, P. Li, C. Chen and Z. Sun, *Appl. Surf. Sci.*, 2014, **319**, 107–112.
38 A. T. Le, S. Y. Pung, S. L. Chiam, N. A. H. BT, N. Josoh, T. Y. Koay, J. S. Lee and N. B. Mustar, *AIP Conf. Proc.*, 2020, **2267**, 020017.
39 A. ul Ahmad, A. Abbas, S. Ali, M. F. e-alam, Z. Farroq, Q. Abbas, M. Ahmad, A. Farid, A. M. afzal, H. M. U. Arshad, M. Javid and M. Iqbal, *Ceram. Int.*, 2021, **47**, 10089–10095.
40 T. Q. Q. Viet, V. H. Khoi, N. T. H. Giang, H. T. V. Anh, N. M. Dat, M. T. Phong and N. H. Hieu, *Colloids Surf., A*, 2021, **629**, 127464.
41 S. Khan, A. Noor, I. Khan, M. Muhammad, M. Sadiq and N. Muhammad, *Catalysts*, 2023, **13**, 44.
42 Y. Sheng, J. Yang, F. Wang, L. Liu, H. Liu, C. Yan and Z. Guo, *Appl. Surf. Sci.*, 2019, **465**, 154–163.
43 A. Sawut, T. Wu, R. Simayi, T. Wu, X. Gong and Z. Wang, *Colloids Surf., A*, 2023, **678**, 132531.
44 A. A. Manda, S. A. Haladu, K. A. Elsayed, U. I. Gaya, M. Alheshibri, A. A. Baroot, E. Çevik, I. Ercan, F. Ercan, T. S. Kayed, S. M. Magami and N. A. Altamini, *Opt. Laser Technol.*, 2023, **160**, 109105.
45 I. J. Badovinac, R. Peter, A. Omerzu, K. Salamon, I. Šarić, A. Samaržija, M. Perčić, I. K. Piltaver, G. Ambrožić and M. Petravić, *Thin Solid Films*, 2020, **709**, 138215.
46 A. Villamayor, T. Pomone, S. Perero, M. Ferraris, V. L. Barrio, E. G. Berasategui and P. Kelly, *Ceram. Int.*, 2023, **49**, 19309–19317.
47 Y. Ji, R. Xiao, X. Tang, W. Chen, J. Wang, F. Long and Z. Zou, *Opt. Mater.*, 2024, **150**, 115335.